Estimating the Spread of Wildland Fires via Evidence-Based Information Fusion

Alexander Soderlund, *Member, IEEE*, and Mrinal Kumar, *Member, IEEE*

***Abstract*— This article presents a new evidential reasoning approach for estimating the state of an evolving wildfire in real time. Given assumed terrain information and localized wind velocity distribution parameters, a probabilistic representation (i.e., the belief state) of a wildfire is forecast across the spatiotemporal domain through a compilation of fire spread simulations. The forecast is updated through information fusion based on observations provided by: 1) embedded temperature sensors and 2) mobile vision agents that are advantageously directed toward locations of information extraction based on the current state estimate. This combination of uncertain sources is performed under the evidence-based Dempster's rule of combination and is then used to enact sensor reconfiguration based on the updated estimate. This research finds that the evidential belief combination vastly outperforms the standard forecasting approach (where no sensor data are incorporated) in the presence of imprecise environmental parameters.**

***Index Terms*— Adaptive estimation, agent-based modeling, estimation theory, evidential reasoning, sensor fusion.**

I. Introduction

IT HAS become evident that there is a need for rapid, real-time estimation of wildfires as their frequency and severity are expected to increase due to warming temperatures and earlier spring snow-melts, particularly along the wildland–urban interface in certain geographic regions [1]. While naturally occurring fires are beneficial to environments that require consistent fire events to maintain the health and diversity of ecosystems [2], uncontrolled wildland fires can be a source of financial and physical losses for communities [3] and a hazard to natural resources and wildlife habitats [4], [5].

Crucially, in the presence of unpredictable environmental conditions, accurate predictions of fire presence are difficult to acquire. In an official report on the Lower North Fork Fire [6], wherein a prescribed fire in Colorado transformed into an uncontrolled wildfire, it was determined that one of the leading causes was "a rapidly escalating wind event" that carried embers across a fire control line. The autopsy report also declared that "weather and fire behavior predictions did not/could not predict the complete set of circumstances that occurred." These sentiments were echoed in a special inquiry report regarding the Margaret River Bushfire [7], an uncontrolled prescribed fire that broke out near Gracetown, Australia, where observed weather conditions were "more extreme than the forecast." An underlying through line of these cases is the presence of *uncertainty* regarding the fire's behavior. When a spreading fire can be feasibly hindered by fire suppression personnel, effective execution of fire suppression methods [8] requires a precise representation of where the fire front currently is and where it is progressing. This representation can be achieved through a real-time, adaptive state estimate of the evolving fire, where the inherent uncertainty of this estimate may be characterized through some stochastic model, also known as its *belief state*. When observation of the system is available, it is desired that the combination of an assumed dynamics model of the system with these observations will yield a state estimate such that the errors between the estimated and true values of the system's states are reduced. A common form of state estimation (see Bayesian filters in [9]) operates through a two-step recursion: 1) propagation of the system's belief state through its assumed dynamics model to a future point in time (i.e., a *prior* belief state) and 2) assimilation of the received measurement data to update the prediction (i.e., a *posterior* belief state) through a step of information fusion. This posterior belief is then utilized for the next round of propagation.

In the context of the wildland fire suppression (and, hence, representation) problem, the recent rise in computational, sensing, and communication capabilities allows us to adopt this recursive state estimation procedure described above by casting the evolving fire front as a random dynamical system whose physical states (e.g., the perimeter positions, flame lengths, and intensity) are propagated through a fire spread dynamics model. These states are then autonomously observed by sensing agents in the field, such as unmanned aircraft systems (also referred to as drones) for data fusion. Furthermore, this work employs the use of *adaptive state estimation* where both the sensing set and the dynamics model can be modified over time. This is useful in a case where the dynamics model of a physical system is driven by a set of input parameters whose values are not truly known (e.g., inadequate wind information or faulty initial ignition locations are given to a fire spread propagator). Furthermore, a set of sensing agents tasked with observing this physical system can be

Manuscript received 26 July 2021; revised 19 February 2022; accepted 14 May 2022. Date of publication 23 June 2022; date of current version 23 February 2023. This work was supported in part by the Air Force Office of Scientific Research under Grant AFOSR 60056837 and in part by the National Science Foundation CNS NRI 3.0 under Award 2132798. Recommended by Associate Editor G. Notarstefano. *(Corresponding author: Alexander Soderlund.)*

Alexander Soderlund is with the National Academy of Sciences/Space Vehicles Directorate, Kirtland Air Force Base, Albuquerque, NM 87123 USA (e-mail: soderlund.3@osu.edu).

Mrinal Kumar is with the Department of Mechanical and Aerospace Engineering, The Ohio State University, Columbus, OH 43235 USA (e-mail: kumar.672@osu.edu).

Color versions of one or more figures in this article are available at https://doi.org/10.1109/TCST.2022.3183645.

Digital Object Identifier 10.1109/TCST.2022.3183645

regularly *reconfigured* based on the predictions of the physical system's states (e.g., drones are routed to frequently predicted fire locations) in order to provide optimal information content (and, hence, reduce the uncertainty of the updated belief state). Once the reconfigured sensing agents have provided data on the system, information regarding the physical system's parameters is obtained, and the accuracy of the dynamics model is improved (e.g., the fire's spread/intensity indicates that wind speeds are higher than anticipated). This refined dynamics model will, in turn, enhance the reconfiguration process of the sensing set (e.g., the updated set of probable fire locations).

Contributions

The primary contributions of this work are the so-called basic belief mappings derived for temperature and vision sensors, and an evidence-based data fusion procedure that uses stochastic fire spread dynamics, which underlies the foundation of a real-time wildfire estimator. In addition to a wildfire belief state, this autonomous estimator also provides locations of interest that can direct mobile aerial observers and ultimately aid effective wildland fire suppression.

Outline

The remainder of this section gives a literature review of the fire characterization methods followed by a brief overview of the fundamental principles of Dempster–Shafer theory (DST), which this work adopts for both belief representation and belief fusion. Section II provides the methodology by: 1) reviewing the Rothermel fire spread model; 2) describing the modeled stochastic spread of a wildfire on a landscape scale; and 3) deriving the bidirectional estimation procedure based on environmental, temperature, and visual data gathered by the wildfire-sensing agents used in this work. The performance of the proposed estimation scheme via numerical simulations is evaluated in Section III. Section IV follows with concluding remarks and some potential avenues for future research.

A. Preliminaries I: Wildfire Characterization

Modern methods of characterizing the spread of wildland fires via mathematical models date back to studies done in the 1940s by Fons [10], [11] and directly influenced the seminal works of Rothermel [12] and Albini [13], [14] who developed an improved model in the 1970s that serves as the basis of many predominantly used fire spread models used today. The inclusion of stochasticity into wildfire expansion has also been extensively studied—see the works of Hargrove *et al.* [15], Catchpole *et al.* [16], Boychuk *et al.* [17], and Krougly *et al.* [18], as well a series of survey papers compiled by Sullivan [19]–[21]. Deficiencies in modern wildfire modeling methods have been tabulated by Alexander and Cruz [22].

The aforementioned approaches can broadly be classified as wildfire *forecasting* based on some set of physical parameters. In an ongoing wildfire scenario, however, the forecast state of the fire may be imprecise and can be augmented by in-the-field observations provided by sensing agents. This act of updating a prior belief state of the fire via measurements into a new belief state representation is what we refer to as wildfire *estimation*. This view is also shared in the 2016 work of Srivas *et al.* [23] who implemented an ensemble Kalman filter to perform data assimilation between an FARSITE-generated forecast and imperfect fire perimeter measurements.

In terms of sensing agents, researchers (see the work of Doolin and Sitar [24]) have demonstrated that a network of wirelessly connected temperature sensors can be used to alert a central receiving station of an encroaching fire front. This has been investigated in recent studies involving automated fire detection through a communicating network of cameras and sensors, such as Alert Wildfire [25]. Furthermore, Pham *et al.* [26] explored the use of mobile vision sensors emplaced on UAVs that tracked a propagating wildfire by maintaining the fire's perimeter within each drone's field of view.

While the adoption of evidential reasoning methods is not exceedingly common in the fields of wildfire science, their use is not unprecedented. Zervas *et al.* [27] proposed the evidence-based fusion of the beliefs provided by immobile temperature and vision sensors in the use of a potential fire detection system although the belief mappings for the vision-based observer are not discussed. Zhao *et al.* [28] used DST to accomplish intracluster belief fusion for groups of temperature sensors. DST was employed in [29] to identify potential occurrence rates of wildfires in fire-prone regions in central Chile, while DST was used in [30] in a postfire event to estimate the extents of burned areas. In these works, the real-time estimation of a spreading fire using evidence-based methods was not the focus although this topic was of interest to previous works of the present authors. In [31], rudimentary forms of belief assignment functions (not used in this work) for immobile temperature and vision-based sensors were discussed but not implemented into a recursive state estimation procedure. In [32], an estimation procedure was realized involving the information fusion of a wildfire forecaster, immobile temperature, and vision agents. This was expanded in [33], where aerial agents were modified to be mobile and observed (albeit primitive) simulated thermal images of an environment. This study is a significant advancement over these previous works in that all sources of "wildfire belief" (the computational forecaster, the temperature agent, and the vision agent) have been overhauled. First, the stochastic fire forecasting models of [31]–[33] were all based on the Markovian spread model of [17], while this work utilizes the more precise Rothermel spread model, which is widely used in the field of wildland fire science. Second, temperature and imaging data obtained from a prescribed burn were used to aid in the derivation of new belief mapping functions for both agents, both of which differ entirely from the assignments utilized in [31]–[33].

B. Preliminaries II: Evidential Reasoning

With the recent rise of autonomous applications, so too has the need arisen for robust and precise automated

decision-making procedures, particularly in the presence of uncertainty. When a decision must be made efficiently while in the presence of multiple sources of (often conflicting) information, the central issue that must be addressed is that of *evidence combination*: how should one fuse the information that is being provided from numerous sources that are all concerned with the same system of interest? In this study, we have adopted information fusion within the DST of probable reasoning, which is a generalization of the conventional Bayesian framework. DST has seen widespread acceptance across numerous disciplines, notably artificial intelligence and decision-making [34]–[39]. Although an overview of this framework is given in this section, a more in-depth explanation and derivation can be found in an extensive review paper from [40] and Shafer's own recent recounting of the theory's development [41].

1) Dempster–Shafer Theory: Consider a question with multiple finite possible explanations (e.g., will it snow over a given city on Christmas day?). The finite set of mutually exclusive and collectively exhaustive *hypotheses* that act as adequate answers to this question is defined as the *frame of discernment*: $\Theta = \{\theta_1, \theta_2, \ldots, \theta_i, \ldots, \theta_n\}$, where exactly one hypothesis θ_i is the truth. A possible frame for the above example could be the binary set $\Theta = \{\text{Snow, No Snow}\}$. Conventionally, modern probability theory (i.e., Kolmogorov's axioms) would treat Θ as an event space and assign a probability to each hypothesis θ_i such that countable additivity is honored. In this toy example, $P(\text{Snow}) = p$ and $P(\text{No Snow}) = 1 - p$, where $p \in [0, 1]$. DST differs from the "additive view" by alternatively allowing the assignment of belief (based on the available evidence) to multiple conflicting hypotheses. Belief is allocated among members, known as *propositions*, of the power set 2^Θ. To continue the snow example: $2^\Theta = \{\emptyset, \text{Snow, No Snow, \{Snow, No Snow\}}\}$. In the DST view, if there is *no information* to support either the "snow" or "no snow" hypotheses (e.g., the city is not given), and then, belief should instead be placed into the "either one is possible" proposition {Snow, No Snow}, as opposed to assuming that they are equally likely $P(\text{Snow}) = P(\text{No Snow}) = 0.5$ as in the conventional view.

The degree of belief that a particular proposition $A \subseteq \Theta$ is true is derived from the current evidence in support of A. This numerical "amount" of belief for any proposition A supplied by an expert E is quantified through the nonnegative, scalar *mass number*, denoted $m_E(A) \in [0, 1]$ such that the sum of all mass numbers satisfies $\sum_{A_i \in 2^\Theta} m_E(A_i) = 1$. The array of mass numbers assigned over the entire frame of discernment is the vector $\mathbf{m}_E \in [0, 1]^{|2^\Theta|}$, defined as

$$\mathbf{m}_E = \big(m_E(\emptyset), m_E(A_1), \ldots, m_E(A_i), \ldots, m_E(\Theta)\big) \quad (1)$$

where we adopt the conventional "closed-world" assumption $m_E(\emptyset) = 0$. A useful example of a common mass assignment function is the *simple support* function defined in the following:

$$m(A) = \begin{cases} s, & \text{if } A = B \\ 1 - s, & \text{if } A = \Theta \\ 0, & \text{otherwise.} \end{cases} \quad (2)$$

It is helpful to envision this assignment process by having each expert initialized from a point of complete ignorance (e.g., $m(\Theta) = 1$) and then reallocating mass away from the ignorance and into a particular proposition $B \subset \Theta$ by a certain amount s when evidence supporting that proposition becomes available. Furthermore, the mass assigned to a proposition composed of multiple hypotheses is not, in general, divisible into the masses of its constituent parts. For example, $m(\Theta) \neq m(\{\theta_1\}) + m(\{\theta_2\}) + \cdots + m(\{\theta_n\})$. Intuitively, any mass for the proposition of *complete ignorance*, $m(\Theta)$, represents the failure of the available evidence to favor any one hypothesis over all of the others.

2) Dempster's Rule: In the case where two independent experts $E1$ and $E2$ each supply their own sets of mass numbers over the power set 2^Θ, the fused belief of any proposition $A \in 2^\Theta$ can be generated via *Dempster's rule of combination* [42]

$$m_C(A) = K \sum_{A_i \cap B_j = A} m_{E1}(A_i) m_{E2}(B_j) \quad (3)$$

where the normalization constant $K = 1/1-\kappa$ is computed from the *degree of conflict* $\kappa \in [0, 1]$ between the masses of the two experts $E1$ and $E2$

$$\kappa = \sum_{A_i \cap B_j = \emptyset} m_{E1}(A_i) m_{E2}(B_j). \quad (4)$$

The generation of this new array of mass numbers is represented in vector form as

$$\mathbf{m}_C = \mathbf{m}_{E1} \oplus \mathbf{m}_{E2}.$$

In general, *conflict* (disagreement between sources) should not be conflated with *ignorance* (the absence of evidence supporting any one proposition over the others). The beliefs of n experts may be combined by applying (3) recursively

$$\mathbf{m}_C = (((\mathbf{m}_{E1} \oplus \mathbf{m}_{E2}) \oplus \mathbf{m}_{E3})) \cdots \oplus \mathbf{m}_{En}$$

as Dempter's rule is associative. The resulting array from performing Dempster's rule on a set of simple supports [defined in (2)] yields what is known as a *separable* support array. Separable support arrays serve as the foundation of the agents' beliefs derived in Section II. We mention here that, since its initial release, several modifications have been proposed to the rule of combination. Yager [43], Dubois and Prade [44], and Zhang [45] have contributed new combination tactics involving the treatment of conflict.

We briefly mention here an extension to DST, known as the transferable belief model (TBM) [46], which maps[1] the epistemic beliefs of the mass number arrays into "pignistic" betting probabilities $P_{\text{Bet}} : \Theta \to [0, 1]$ computed as

$$P_{\text{Bet}}(\theta_i) = \sum_{\theta_i \in A \subseteq \Theta} \frac{m(A)}{|A|} \quad (5)$$

where $|A|$ is the number of singleton hypotheses θ_i that belong in the set A. In addition, the betting probabilities satisfy

[1]This mapping is rooted in the principle of insufficient reasoning. An extensive discussion regarding the validity of the TBM is provided in [47].

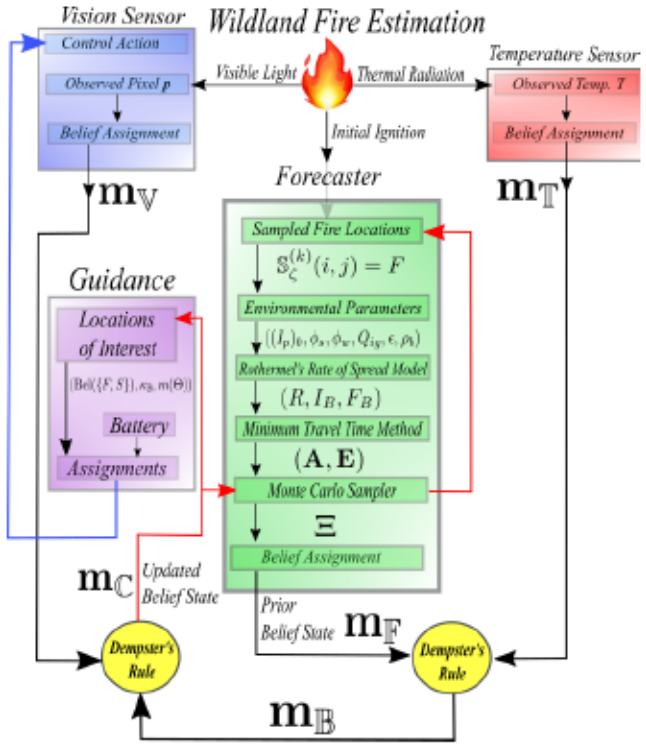

Fig. 1. Bidirectional feedback procedure reframed for the wildfire estimation application.

Kolmogorov's axioms

$$\sum_{\theta_i \in \Theta} P_{\text{Bet}}(\theta_i) = 1$$

$$P_{\text{Bet}}(\emptyset) = 0.$$

II. Methodology: Adaptive State Estimation

This section introduces the three types of agents that assign degrees of belief regarding the fire: 1) the forecaster; 2) the temperature sensor; and 3) the mobile vision sensor. These are, respectively, represented by the green, blue, and red blocks in Fig. 1. These three sources of information assign environmental state beliefs based on their interpretation of the available data:

1) the computational "forecaster" that predicts the environmental belief state at every location for future times via aggregating numerous fire propagation simulations;
2) the thermal sensor agent that indirectly detects the surrounding fire's presence via the increase in ambient temperature readings;
3) the airborne vision sensor agent that uses rudimentary pattern recognition to classify vegetation, flames, and ash within its field of view.

All sources listed above are imperfect. While the forecaster provides offers evidential information for all locations simultaneously, its precision is reliant on accurate wind, terrain, and ignition location data, which may not be available. The thermal sensor, while adept at indicating temperature anomalies, suffers from saturation and only provides environment information at a single location. The aerial vision sensor requires tuning via extensive data collection based on the operating environment but, on a practical level, has limited availability due to power (i.e., flight time) constraints. Their measurements are the lens through which the actual fire is perceived that the forecaster does not have access to and serve as the foundation for updating the beliefs originally issued by the forecaster. The temperature sensor is particularly useful in scenarios where the assumed environmental conditions input to the forecaster are incorrect. The beliefs of these agents are combined to produce an updated belief state regarding the fire, which is then fed back into the forecasting agent to enhance its precision for future fire propagation (red arrow in Fig. 1). This updated belief is also used to generate current locations of interest in the environment. These "survey spots" are then routed to the mobile vision sensor as guidance actions (blue arrow in Fig. 1) that are explored in Section II-D.

We define the frame of discernment adopted for the wildland fire application as follows:

$$\Theta = \{\text{Vegetation}(V),\ \text{Fire}(F),\ \text{Nonburnable}(S)\}.$$

This yields the power set of propositions

$$2^{\Theta} = \{\emptyset,\ V, \{V, F\},\ F, \{F, S\},\ S,\ \{V, S\},\ \Theta\}.$$

The hypotheses $\{V, F, S\}$ describe what state a given location within the wildfire environment is predominantly experiencing at any given time. For instance, a location initially composed entirely of combustible wildland fuel is designated V. Sometime later, it may transition to F if it becomes a segment of the growing surface fire perimeter. Once the energy of the fuel is expended, it will then transition into the ash state (S), which is modeled as nonburnable. Noncombustible environmental features, such as water, are also set to S. Assigning beliefs into which locations can: 1) potentially burn; 2) are burning; and 3) cannot burn is critical to characterizing the wildland fire's evolution and benefits evidence-based decision-making.

A. Belief Model I: Wildland Fire Forecaster

Given the assumed ignition points that a spreading fire originates from, a computational forecaster employs the modeled dynamics of wildfire spread in order to yield a degree of belief that the fire will arrive at a certain location and time based on a series of input parameters (surface wind velocity, local topography, types of vegetative fuel, humidity, and so on) that drive the fire's growth. This degree of belief regarding a given location's condition is given in the form of the mass number array $\mathbf{m}_{\mathbb{F}}$ and is derived from the occurrence rate (i.e., frequency) of fire presence.

In order to adequately model the dynamics of the physical system, this work employs the highly used model developed by Rothermel [12] and Andrews [48] that approximate a fire's spread based on local environmental inputs of topography, wind velocity, and combustible fuel

$$R = \frac{I_R \xi_R (1 + \phi_w + \phi_s)}{\rho_b \varepsilon Q_{ig}} \tag{6}$$

where the numerator (heat source) is composed of the total reaction intensity I_R, the propagating flux ratio ξ_R, and the

dimensionless wind and slope amplification factors, ϕ_w and ϕ_s. The denominator (heat sink) is the amount of heat required for ignition Q_{ig} multiplied by the bulk density ρ_b (i.e., amount of oven-dry fuel) and the dimensionless effective heating number $\varepsilon \in [0, 1]$, which signifies the proportion of the fuel that is ignited ahead of the fire's leading edge (e.g., fine fuels have values closer to unity). This deterministic model is applicable to local (and static) environmental parameters. This spreading model can be extended to operate across a complex landscape by representing the entire wildfire environment as a time-varying $m \times n$ array, wherein each element of the lattice, $\mathbb{S}^{(k)}(i, j)$, represents the state of the Cartesian coordinate (i, j) at timestep k and is described by one of three discrete values: $\mathbb{S}^{(k)}(i, j) \in \{\text{Fuel, Fire, Ash/Nonburnable}\}$. It follows that the state of the environment at time k is denoted as

$$\mathbf{S}^{(k)} = \begin{bmatrix} \mathbb{S}^{(k)}(1,1) & \dots & \mathbb{S}^{(k)}(1,n) \\ \vdots & \ddots & \vdots \\ \mathbb{S}^{(k)}(m,1) & \dots & \mathbb{S}^{(k)}(m,n) \end{bmatrix}.$$

By compiling fuel, wind, and slope information at each node, an array that tabulates the maximum rate of spread from each location via (6) is created. In the case where environmental conditions are static across the landscape, the minimum travel time (MTT) method developed by Finney [49] treats the minimum time required for the fire to travel from a node (i_1, j_1) to any other node (i_2, j_2) as a weighted edge between two vertices of a graph. Since these "weights" represent differential times, any node(s) set as the initial ignition points at time $k = 0$ will then yield the fire arrival times to all nodes by implementing a shortest-path (i.e., minimum-time) algorithm, such as the classic technique developed by Dijkstra *et al.* [50]. Fig. 2(a) displays an example of fire travel trajectories output by the MTT method from a single ignition point. Fig. 2(b) displays the location of the merged fire front at a series of timesteps based on the paths of MTT in Fig. 2(a).

Due to the presence of stochastic environmental conditions, predominantly witnessed through time-varying surface wind velocities (see [51]), this work assumes that the local wind speed and direction at each node vary according to an assumed distribution. For example, the wind speed at any node, $w_s(i, j)$, can be sampled from a uniform probability distribution, $w_s(i, j) \sim \mathscr{U}(w_\ell(i, j), w_u(i, j))$, where $w_\ell(i, j)$ and $w_u(i, j)$ are the respective lower and upper wind speeds *predicted* to occur at (i, j) over the simulation time. Given the set of initial ignition points and the distributions of potential parameters at each location, we may apply a Monte Carlo method (see [52]), where the environmental inputs are sampled from these distributions, and a single "run" of the MTT algorithm is performed. The compilation of runs up to time τ may be denoted $\{\mathbf{S}_1^{(\tau)}, \mathbf{S}_2^{(\tau)}, \dots, \mathbf{S}_\zeta^{(\tau)}, \dots, \mathbf{S}_Z^{(\tau)}\}$, and the completion of Z simulations will yield the aggregated spatiotemporal frequentist chance for state $\theta \in \{\text{Fuel, Fire, Ash/Nonburnable}\}$ to occur at time k as

$$q_\theta^{(k)}(i, j) = Z^{-1} \sum_{\zeta=1}^{Z} \{1 \mid \mathbb{S}_\zeta^{(k)}(i, j) = \theta\} \tag{7}$$

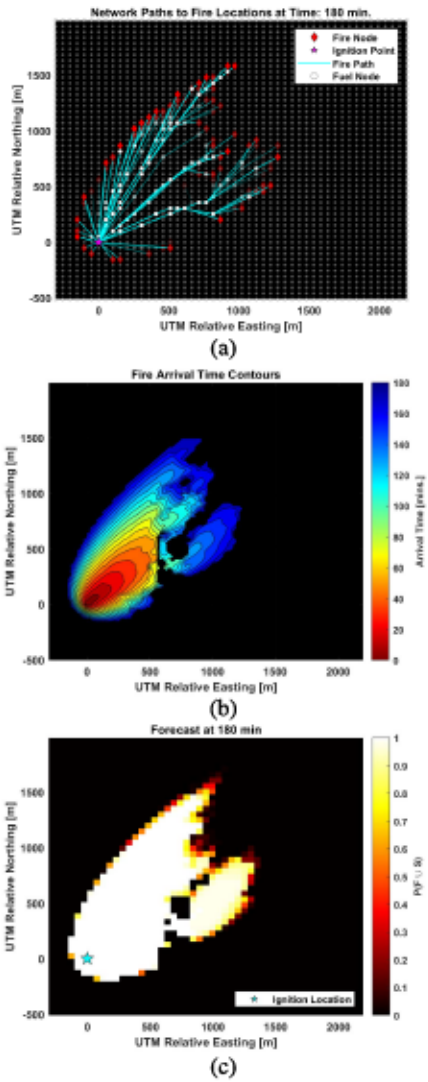

Fig. 2. (a) Associated network analogy that shows the paths that the fire (under southwesterly winds) took from a single ignition point in the southwest corner of the landscape at $k = 0$ to the current fire locations at $k = 180$ min. (b) Interpolated time contours of the fire front based on the network output. Easting and northing coordinates are relative to the ignition location. (c) Forecast of "burn probability" using $\Xi^{(k)}$ at the time of 180 min.

and a resulting "frequentist chance" array $\Xi^{(k)}$ of size $m \times n$ can be constructed

$$\Xi^{(k)} = \begin{bmatrix} \xi^{(k)}(1,1) & \dots & \xi^{(k)}(1,n) \\ \vdots & \ddots & \vdots \\ \xi^{(k)}(m,1) & \dots & \xi^{(k)}(m,n) \end{bmatrix} \tag{8}$$

where each element is the probability mass function $\xi^{(k)}(i, j) = [q_{\text{Fuel}}^{(k)}(i, j), q_{\text{Fire}}^{(k)}(i, j), q_{\text{Ash}}^{(k)}(i, j)]^T$. Fig. 2(c) displays the frequentist "burn probability" [i.e., $q_{\text{Fire}}^{(k)}(i, j) + q_{\text{Ash}}^{(k)}(i, j)$] based on aggregated runs simulated over a range of conditions for the environment used for the simulation in Fig. 2(b).

The mapping from the array of frequentist values $\xi(i, j)^{(k)}$ to the mass number array $\mathbf{m}_{\text{F}}^{(k)}$ is constructed as an array of separable supports. To do this, we generate a set of simple

(a)

(b)

Fig. 3. (a) Temperature sensor placed prior to a prescribed burn event in Marion, OH, USA. (b) Temperature readings transmitted by this sensor during the burn event. In this particular case, the flame front passed directly underneath the sensor's position (about 2 m above ground) and caused no physical damage.

supports $\mathbf{m}_{\mathbb{F}-\theta}^{(k)}$ for each corresponding singleton state θ

$$m_{\mathbb{F}-\theta}^{(k)}(A) = \begin{cases} q_\theta^{(k)}, & \text{if } A = \theta \\ 1 - q_\theta^{(k)}, & \text{if } A = \Theta \\ 0, & \text{otherwise.} \end{cases} \tag{9}$$

The mass arrays of all subexperts are combined via Dempster's rule (3) to create the comprehensive separable set of beliefs for the forecasting agent at location (i, j) and time k

$$\mathbf{m}_{\mathbb{F}}^{(k)} = \mathbf{m}_{\mathbb{F}-V}^{(k)} \oplus \mathbf{m}_{\mathbb{F}-F}^{(k)} \oplus \mathbf{m}_{\mathbb{F}-S}^{(k)}. \tag{10}$$

B. Belief Model II: Temperature Sensor

The increase in temperature due to a moving fireline's radiating heat flux can be observed by immobile ground-based temperature sensing agents. These agents, placed at various locations throughout the environment, are treated as nodes within a wireless network that all transmit ambient temperature measurements of their respective positions at a constant rate to some central processing unit responsible for data acquisition and decision-making. The network is physically represented as a binary lattice $\mathbb{T}^{(k)}$ of size $m \times n$, where $\mathbb{T}^{(k)}(i, j) = 1$, if a temperature agent is reporting data from location (i, j) at time k. Fig. 3(a) depicts a temperature sensor in use, while Fig. 3(b) shows its corresponding temperature readings during a prescribed burn event.

While operating in the field, a temperature agent "activates" if its local ambient temperature surpasses some threshold (e.g., 35 °C), which is interpreted as evidence of an approaching fire front.[2] As the sensor is expected to saturate at some temperature, e.g., the agent in Fig. 3 cannot measure temperatures above 120 °C, this limit presents difficulties in determining the precise time of fire passage as a "hot" reading alone does not distinguish between three possibilities: 1) the vegetation is heating up, i.e., fire is approaching; 2) the fuel bed is actively burning, i.e., fire is present; and 3) hot ash is cooling, i.e., fire has passed. To construct the beliefs of the agent, one can incorporate additional information, such as the *amount of time*, in which the sensor has been above a threshold temperature and the predicted behavior of wildland fire based on the (assumed) environmental parameters.

The characteristics (e.g., height, speed) of the approaching fire front affect the rate of increase of the sensor's temperature surroundings due to the fire's radiating heat flux. The contiguous wall of flame is treated as a radiative surface (see [53]) that emanates a heat flux at a rate according to the Stefan–Boltzmann law

$$E = \epsilon_s \sigma_s T^4 \tag{11}$$

where T is the absolute temperature in K, ϵ_s is the emissivity, and $\sigma_s = 5.67 \times 10^{-8}\ W/m^2K^4$ is Stefan–Boltzmann's constant. When calculating the radiative heat transfer between any two surfaces, it is crucial to consider the view factor, F_{1-2}, a dimensionless quantity between 0 and 1, which represents the fraction of the radiation that leaves surface 1 and strikes surface 2. Under the assumption that the surrounding heat aura around the temperature agent acts as an *enclosure*, the configuration factor F_{1-2} between two surfaces can be approximated via the method employed by [54] to determine wildland firefighter safety zones

$$F_{1-2} = \frac{1}{A_1} \int_{A_1} \int_{A_2} \frac{\cos(\mu_1)\cos(\mu_2)}{\pi S^2} dA_2 dA_1 \tag{12}$$

where A_1 and A_2 are the areas of the two respective surfaces, μ_1 and μ_2 are the respective angles between the surface normal vectors $\hat{\mathbf{n}}_1$ and $\hat{\mathbf{n}}_2$, and S is the distance between the differential areas, as shown in Fig. 4(a).

A fuel model and effective wind speed pairing will generate both the surface rate of spread R and associated flame height F_H. Subsequently solving (12) over varying values of the surface distance S, the incident radiant heat flux on the sensor's surface can be found [see Fig. 4(b)]. A sensor's simulated temperature response can be approximated by solving the radiation dynamics as the flame surface approaches and then exponentially cooling the observed temperature to an updated ambient temperature once the fire front has passed. Thus, a series of temperature readings over an activation period of τ timesteps $\mathbf{T}_h = [T_h^1, \ldots, T_h^{(k)}, \ldots, T_h^\tau]$ can be generated for *each* headfire spread rate within a given range $R_h \in [R_{\min}, R_{\max}]$. Fig. 5(a) displays the temperature responses of an impervious sensor as it encounters a front progressing at either end of the spread rate range.

[2]Headfire rates of spread are assumed for modeling purposes, but flank ($\nu = \pi/2$) and back ($\nu = \pi$) fires also yield higher air temperatures.

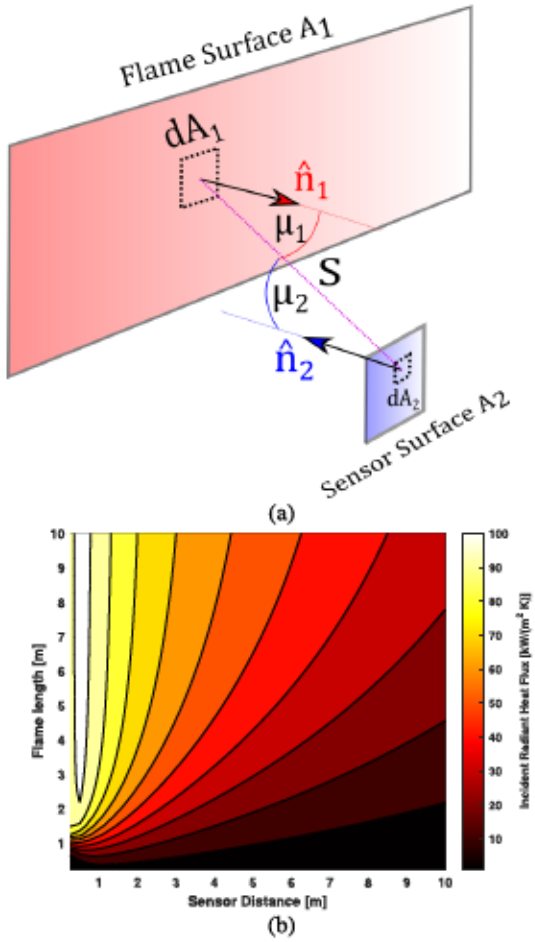

Fig. 4. (a) Flame front and the temperature agent are modeled as radiating rectangular surfaces. (b) Radiative heat flux incident on the temperature sensor surface as a function of: 1) sensor's distance away from the flame front and 2) front's flame height.

By cataloging the actual environmental states of the sensor's location $\mathbb{S}^{(k)}(i, j)$ for each spread rate R_h and activated time $T_h^{(k)}$, a frequentist chance value of proposition A at each time can be obtained as

$$q_A^{(k)} = \frac{\sum_{i\in m}\sum_{j\in n}\{1 \mid \mathbb{S}^{(k)}(i,j) \subseteq A\}}{\sum_{i\in m}\sum_{j\in n}\{\mathbb{T}^{(k)}(i,j)\}}. \tag{13}$$

Furthermore, the set of simple supports [see (2)] for each subexpert at each time can be constructed as

$$m_{\mathrm{T}-B}^{(k)}(A) = \begin{cases} q_B^{(k)}, & \text{if } A = B \\ 1 - q_B^{(k)}, & \text{if } A = \Theta \\ 0, & \text{otherwise.} \end{cases} \tag{14}$$

The internally combined set of beliefs for the temperature agent $\mathbf{m}_{\mathrm{T}}^{(k)}$ is computed as

$$\mathbf{m}_{\mathrm{T}}^{(k)} = \mathbf{m}_{\mathrm{T}-V}^{(k)} \oplus \mathbf{m}_{\mathrm{T}-\{V,F\}}^{(k)} \oplus \mathbf{m}_{\mathrm{T}-F}^{(k)} \oplus \mathbf{m}_{\mathrm{T}-\{F,S\}}^{(k)} \oplus \mathbf{m}_{\mathrm{T}-S}^{(k)}. \tag{15}$$

The combined mass numbers $m_{\mathrm{T}}^{(k)}(A)$ for a range of headfire spread rates are shown in Fig. 5. Note that belief is apportioned to all feasible propositions through the frequentist chances created via (13), which indicates evidence that points to mutually exclusive states simultaneously.

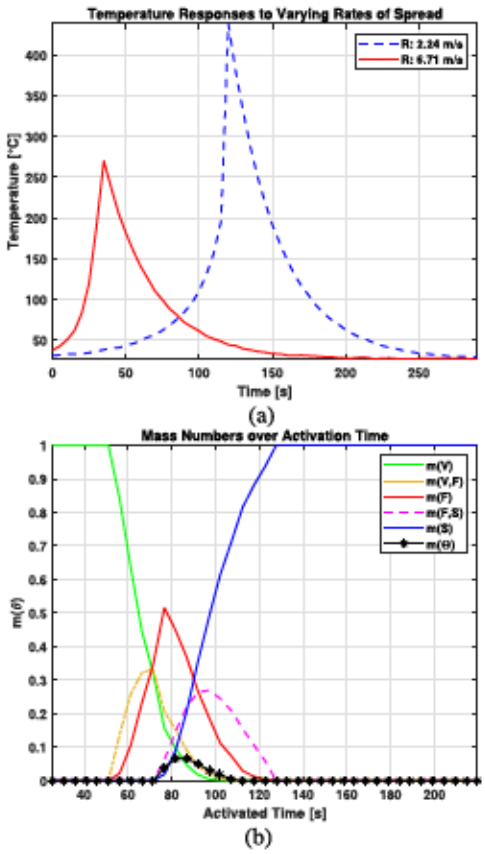

Fig. 5. (a) Temperature response when encountering a flame front with the highest and lowest spread rates. (b) Mass numbers for each proposition $m_{\mathrm{T}}^{(k)}(A)$ over the temperature agent's activation time.

C. Belief Model III: Aerial Vision Sensor

Unlike their temperature-sensing counterparts in Section II-B, the airborne vision agents are mobile sensors that are sent to specific coordinates and survey numerous points within the environment simultaneously. This work assumes that this sensing set is sparse—where the fleet of available drones includes less than ten members. We model the vision agent based on the capabilities of the DJI Mavic 2 Pro, which was recently utilized by the author's research group during a prescribed burn.

Each agent can maneuver with a maximum airspeed of 15 m/s and is equipped with a down-facing camera to capture images that can be routed to a central ground station via a down-link transfer, which are used to update the current fire belief state. The primary drawbacks of this agent are: 1) its energy requirements with approximately 30 min of battery life and 2) its observations can be obscured by smoke and debris.[3]

The physical layout of the vision sensing set is similar to the temperature agent network described above, where the lattice $\mathbb{V}^{(k)}$ is of size $m \times n$, where $\mathbb{V}^{(k)}(i, j) = 1$ if a vision agent is reporting data from location (i, j) at time k. The field of view of each agent's down-facing camera centered at position (i, j) at time k will result in an image $\mathbb{I}^{(k)}(i, j)$ of

[3]Thermal imaging cameras have also been previously modeled by the authors, as in [33].

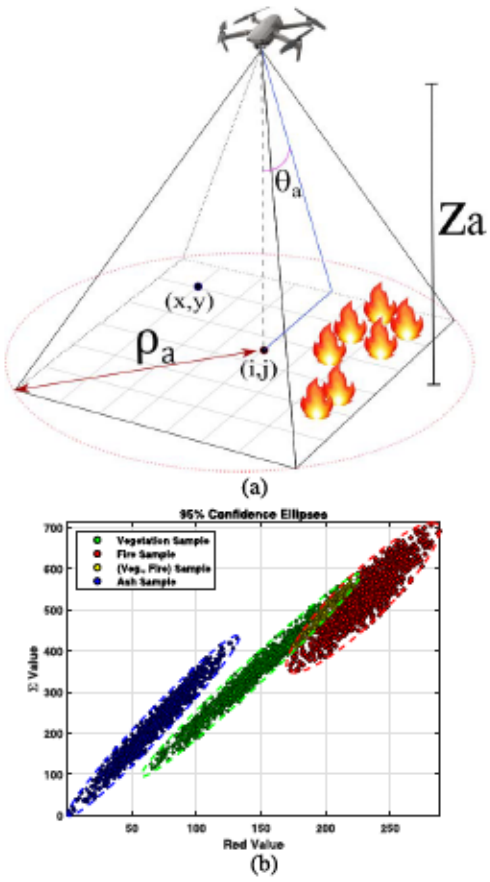

Fig. 6. (a) Field of view provided by a visual agent at an elevation z above the surface. (b) Recognizable states of a wildfire environment are categorized as bivariate distributions over image pixel information.

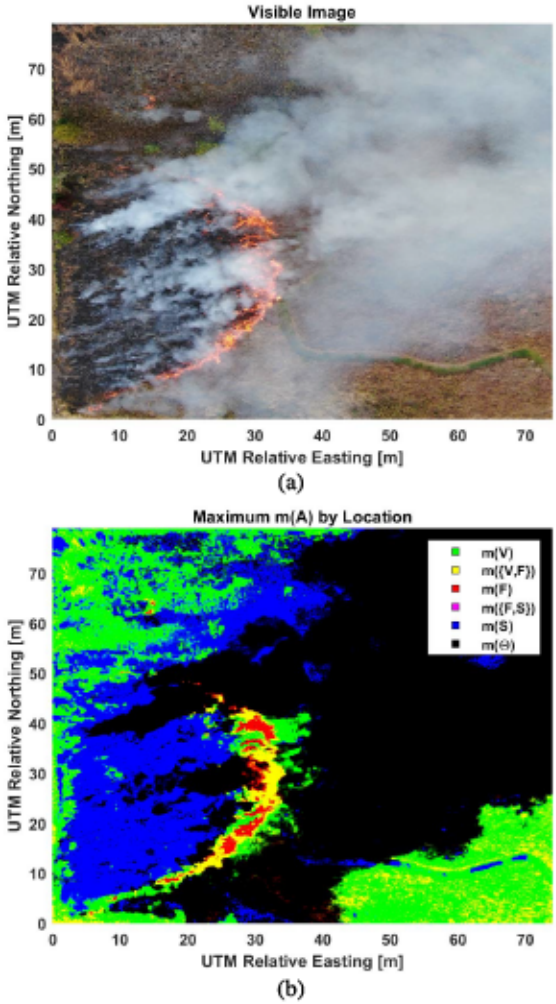

Fig. 7. (a) Visible image of a fire front is captured with a DJI Mavic 2 drone at an altitude of 120 m during a prescribed burn event in Marion. (b) Proposition of highest belief Bel(A) that each pixel contains based on the vision agent's assignments through (17) and (18) of the underlying color intensity data.

the landscape. When aligned with a globally fixed frame, the pixel data contained at image coordinate (x, y) can be used to yield belief state information at the pixel's corresponding landscape location(s). The employment of multiple aerial agents invites carries two considerations: 1) the possibility of mid-air collisions and 2) the optical capture of redundant ground information. To avoid these, a (lateral) distance ρ_a is defined as the radius of the circle, which circumscribes each agent's square observation field [see Fig. 6(a)]

$$\rho_a = \sqrt{2} z_a \tan(\theta_a)$$

and is utilized as a loose constraint when issuing flight trajectories to the agents. Note that "loose" in this context refers to the fact that, in this work, agents are allowed to temporarily pass through each other's airspace, but final target locations are selected such that fields of view do not intersect.

This work assumes that the digital camera housed on each mobile agent captures and stores the received visible light information through the additive RGB color model where every pixel at image location (x, y) and time k contains the array of red, green, and blue intensity values $[\text{Red}^{(k)}(x, y), \text{Green}^{(k)}(x, y), \text{Blue}^{(k)}(x, y)]^T$. The received color array of a location (x, y) is mapped to a corresponding set of mass numbers $\mathbf{m}_{\mathbf{V}}^{(k)}$. It is well-known that certain environmental features display particular color signatures [55].

Consider a set of pixels whose image contents all correspond to the same environmental state (e.g., fire). As each color component c of the received array takes on a value of $c \in [0, 255]$, that state will elicit a combination of color components that, while not the same across all pixels in this set, will tend to conform to a distribution. For example, pixels containing flames shown in Fig. 7(a) tend to contain red values $\text{Red}^{(k)}(x, y) \in [175, 255]$ and total intensity values $\Sigma_{\text{RGB}}^{(k)}(x, y) \in [350, 700]$ where

$$\Sigma_{\text{RGB}}^{(k)}(x, y) = \text{Red}^{(k)}(x, y) + \text{Green}^{(k)}(x, y) + \text{Blue}^{(k)}(x, y).$$

Thus, the data in pixel (x, y) at time k can be modeled as the pair of random variables $\mathbf{p}^{(k)}(x, y) = (\text{Red}^{(k)}(x, y), \Sigma_{\text{RGB}}^{(k)}(x, y))$. This pair of variables (the red intensity value and the sum of the intensity values) was converged upon as an appropriate tool for state classification

and component values corresponding to the three singleton state hypotheses $\{V, F, S\}$ tabulated from 600 frames of a 2-min 4k video captured during a prescribed burn test. The component data for each hypothesis θ can be statistically fit to a bivariate Gaussian distribution $\mathcal{N}_\theta(\hat{\mathbf{p}}_\theta, \mathbf{C}_\theta)$, where $\hat{\mathbf{p}}(\theta)$ is the sample mean vector of the red and total intensity values, and $\mathbf{C}_\theta$ is the sample covariance. Fig. 6(b) displays the 95% confidence ellipses of the proposition distributions

$$\{\mathcal{N}_S(\hat{\mathbf{p}}_S, \mathbf{C}_S), \mathcal{N}_{\{V,F\}}(\hat{\mathbf{p}}_{\{V,F\}}, \mathbf{C}_{\{V,F\}}), \mathcal{N}_F(\hat{\mathbf{p}}_F, \mathbf{C}_F), \mathcal{N}_V(\hat{\mathbf{p}}_V, \mathbf{C}_V)\}$$

along the (Red, Σ_{RGB}) axes corresponding to the blue, yellow, red, and green sample sets, respectively. Crucially, there exists a tangible overlap between the vegetation and fire bivariate distributions. Color component observations that reside in this intersection can be aggregated in order to form a sample mean and covariance for the proposition $\{V, F\}$. In practice, this refers to the case where the information of an observed pixel, $\mathbf{p}^{(k)}(x, y)$, is evidence for both the vegetation and fire hypotheses.

A pixel observation $\mathbf{p}^{(k)}(x, y)$ at any location in the agent's image $(x, y) \in \mathbb{I}^{(k)}(i, j)$ will be some statistical distance (e.g., the Mahalanobis distance metric [56]) away from each state proposition distribution $\mathcal{N}_A(\hat{\mathbf{p}}_A, \mathbf{C}_A)$

$$\mathscr{M}_A^{(k)}(x, y) = \sqrt{(\mathbf{p}^{(k)}(x, y) - \hat{\mathbf{p}}_A)^T \mathbf{C}_A^{-1} (\mathbf{p}^{(k)}(x, y) - \hat{\mathbf{p}}_A)}. \quad (16)$$

This can then be used to assign mass numbers

$$m_{\text{V}-B}^{(k)}(A) = \begin{cases} \exp\left(-C_A \mathscr{M}_A^{(k)}\right), & \text{if } A = B \\ 1 - \exp\left(-C_A \mathscr{M}_A^{(k)}\right), & \text{if } A = \Theta \\ 0, & \text{otherwise} \end{cases} \quad (17)$$

where C_B is some proposition-dependent positive scaling parameter. As in Sections II-A and II-B, each simple support set $\mathbf{m}_{\text{V}-A}^{(k)}$ is combined through Dempster's rule to yield the vision agent's mass number array

$$\mathbf{m}_{\text{V}}^{(k)} = \mathbf{m}_{\text{V}-V}^{(k)} \oplus \mathbf{m}_{\text{V}-\{V,F\}}^{(k)} \oplus \mathbf{m}_{\text{V}-F}^{(k)} \oplus \mathbf{m}_{\text{V}-S}^{(k)}. \quad (18)$$

The results of these total belief assignments are displayed in Fig. 7, where the vision sensor's mass numbers at each location in Fig. 7(b) are derived from the pixel data given from the actual image in Fig. 7(a). This "belief image" demonstrates three important concepts.

1) *Recognition:* High belief values are correctly placed into locations containing ash, fire, and unobscured grassland.
2) *Ambiguity:* Locations along with the fire–grass interface and red-colored fuel will result in belief assignment to the $\{V, F\}$ proposition.
3) *Ignorance:* Pixels where the smoke is thick enough to obscure the color information of the landscape underneath will result in locations with high degrees of ignorance $m(\Theta)$, represented as the black locations in Fig. 7(b).

We mention that the assignment process given through (17) and (18), as well as the selection of tuning parameters C_B, is currently environment-dependent. It is difficult to assess how the use of the pixel information $\mathbf{p}^{(k)}(x, y) = (\text{Red}^{(k)}(x, y), \Sigma_{\text{RGB}}^{(k)}(x, y))$ as the basis for classification (and therefore belief assignment) extends to numerous environments (e.g., fire in grassland versus fire in a woodland). The colors elicited by wildland fire are broadly consistent (see [55]) although universal vegetation and ash identification may require a more advanced feature extraction process. Simply put, additional empirical studies are needed at this time although the principles of the process are sound—visual belief assignments should be based on received data that are state-identifying. Note that (15) and (18) use beliefs applied to "feasible" propositions as neither the temperature nor the vision agent uses simple support functions involving the $\{V, S\}$ proposition. The lack of evidential crossover [see Figs. 5(b) and 6(b)] between the vegetation and ash states is the consequence of the data obtained from the specific environment and is not applicable in general.

D. Bidirectional Feedback Procedure

The estimation procedure of this work is designed as a discrete-time estimator where the dynamics of the fire are modeled over a sequence of regularly spaced timesteps: $k = 0, 1, 2, \ldots, k_f$. The measurements (i.e., temperature and vision beliefs) are also provided at (generally irregularly spaced) discrete timesteps. To invoke the flowchart of Fig. 1 once more, the output of the forecasting block (the prior belief $\mathbf{m}_{\text{F}}^{(k)}$) for each location is combined with the beliefs of available agents through two successive applications of Dempster's rule

$$\mathbf{m}_{\text{C}}^{(k)} = \mathbf{m}_{\text{V}}^{(k)} \oplus \left(\mathbf{m}_{\text{T}}^{(k)} \oplus \mathbf{m}_{\text{F}}^{(k)}\right). \quad (19)$$

As (19) is applied[4] across every location (i, j), the *updated belief state* of the entire environment is constructed as the array

$$\mathbf{B}_{\text{C}}^{(k)} = \begin{bmatrix} \mathbf{m}_{\text{C}}^{(k)}(1, 1) & \cdots & \mathbf{m}_{\text{C}}^{(k)}(1, n) \\ \vdots & \ddots & \vdots \\ \mathbf{m}_{\text{C}}^{(k)}(m, 1) & \cdots & \mathbf{m}_{\text{C}}^{(k)}(m, n) \end{bmatrix} \quad (20)$$

where $\mathbf{B}_{\text{C}}^{(k)}$ is a nonnegative array of size $m \times n \times |2^\Theta|$. An obvious trajectory design question is *where* to send aerial agents based on the current state of domain knowledge. While numerous evidential metrics exist (e.g., ignorance) to drive the sensor reconfiguration, this work has opted to route sensors to locations of the highest postfusion conflict. Intuitively, the disagreement between any two agents implies that, while they are perceiving the same system of interest, one (possibly faulty) agent is providing a significantly different interpretation of the evidence. Let $\kappa(i, j)_k$ be the conflict at location (i, j) and time k. A set of N_d drones can be directed toward the corresponding N_d highest conflict locations $\{(i_1, j_1), (i_2, j_2), \ldots, (i_{N_d}, j_{N_d})\}$, where

$$\kappa(i_1, j_1)_k \geq \kappa(i_2, j_2)_k \geq \cdots \geq \kappa(i_{N_d}, j_{N_d})_k.$$

[4]In the instances where either agent T or agent V is not available to provide beliefs for combination, it is given the so-called "vacuous" mass number array where $m_E^{(k)}(\Theta) = 1$, and all other mass numbers are set to 0.

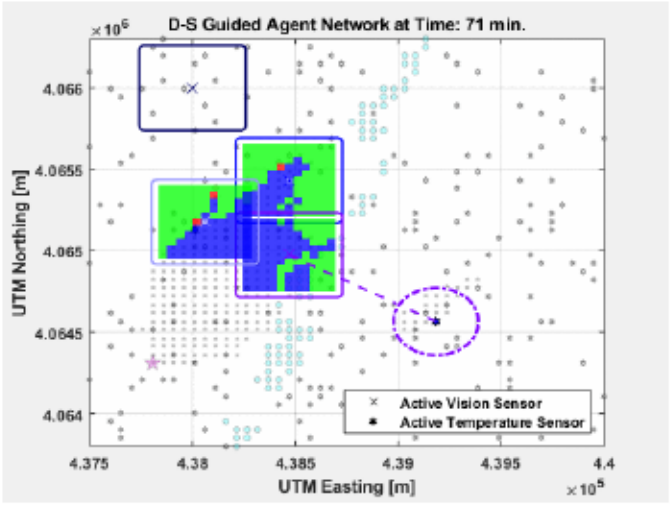

Fig. 8. Top-down view of agent operations.

Consider the following conflict-driven example. In the scenario shown in Fig. 8, three drones (whose fields of view are represented as the rectangles containing red, green, and blue squares) are observing a wildfire that has been growing to the northeast for 71 min. Red squares represent observed burning locations (i.e., $m_{\mathbf{V}}(F)$ is the maximum mass number in $\mathbf{m}_{\mathbf{V}}$), green squares are observed vegetation, and blue squares are observed ash locations. At this timestep, a temperature sensor in the eastern portion of the environment (black star) is activated due to the radiation induced by a second (previously unforeseen) wildfire. As the forecaster had not anticipated this event, the forecaster's high (and incorrect) vegetation mass number $m_{\mathbf{F}}(V)$ is fused with the temperature agent's comparatively lower quantity $m_{\mathbf{T}}(V)$, which results in a nontrivial conflict value $\kappa_{\mathbf{B}}$. One of the three vision agents in the environment (agent d) is then reassigned to this location (i_d, j_d), represented by the dashed purple line, which dictates the sensor's current path of travel. The complete estimation procedure is given in Algorithm 1. The output of this algorithm is the combined belief lattice $\mathbf{B}_{\mathbf{C}}^{(k)}$ at a given timestep k.

Algorithm 1 Fire Estimation-driven Sensor Reconfiguration Algorithm (FESRA)

Require: Fuel $f(i,j)$, Wind $(w_s(i,j), w_d(i,j))$, Slope $\eta(i,j)$
for all Locations (i,j) **do** ▷ Acquire the beliefs of the fire forecasting agent.
  for all $\zeta \in Z$ **do**
    $v \leftarrow 0, f \leftarrow 0, s \leftarrow 0$
    if $\mathbb{S}_{\zeta}^{(k)}(i,j) = V$ **then**
      $v \leftarrow v+1$
    else if $\mathbb{S}_{\zeta}^{(k)}(i,j) = F$ **then**
      $f \leftarrow f+1$
    else if $\mathbb{S}_{\zeta}^{(k)}(i,j) = S$ **then**
      $s \leftarrow s+1$
    end if
  end for ▷ Determine frequentist chance that $\mathbb{S}^{(k)}(i,j) = \theta$
  $\xi^{(k)}(i,j) \leftarrow \frac{1}{Z}[v,\ f,\ s]$
  $\xi^{(k)}(i,j) \rightarrow \mathbf{B}_{\mathbf{F}}^{(k)}(i,j)$ ▷ Create prior belief state.
end for
for all $\{(i,j) | \mathbb{T}^{(k)}(i,j) = 1\}$ **do** ▷ Acquire beliefs of each active temperature agent.
  $T^{(k)} \rightarrow \mathbf{m}_{\mathbf{T}}^{(k)}$ for location (i,j)
end for
for all $\{(i,j) | \mathbb{V}^{(k)}(i,j) = 1\}$ **do** ▷ Acquire the beliefs of each active vision agent.
  for all Locations (x,y) in agent's image $\mathbb{I}^{(k)}(i,j)$ **do**
    $(\text{Red}^{(k)}(x,y),\ \Sigma_{RGB}^{(k)}(x,y)) \rightarrow \mathbf{m}_{\mathbf{V}}^{(k)}$ for location (i,j)
  end for
end for
$\mathbf{m}_{\mathbf{B}}^{(k)} \leftarrow \mathbf{m}_{\mathbf{F}}^{(k)} \oplus \mathbf{m}_{\mathbf{T}}^{(k)}$ for location (i,j), Record $\kappa_{\mathbf{B}}$
$\mathbf{B}_{\mathbf{C}}^{(k)}(i,j) \leftarrow \mathbf{m}_{\mathbf{V}}^{(k)} \oplus \mathbf{m}_{\mathbf{B}}^{(k)}$ for location (i,j) ▷ Create updated belief state.
$\mathbf{B}_{\mathbf{C}}^{(k)} \rightarrow \{\kappa_{\mathbf{B}}, m_{\mathbf{C}}(\Theta), \mathbf{m}_{\mathbf{C}}(\{F,S\})\}$ ▷ Generate guidance metrics
$\{\kappa_{\mathbf{B}}, m_{\mathbf{C}}(\Theta), \mathbf{m}_{\mathbf{C}}(\{F,S\})\} \rightarrow \mathbb{V}^{(k)}(i,j)^*$ ▷ Reassign to $(i,j)^*$
return $\mathbf{B}_{\mathbf{C}}^{(k)}$

III. Results: Simulated Wildland Fire Near Taos, New Mexico

This study features two numerically simulated fires over a discretized representation of a real location near Taos, New Mexico. To evaluate how this work's adaptive estimation process would proceed given a wildland fire event, two characterization methods are employed. The first approach is the collection of beliefs assigned by the temperature sensing set at each timestep. By design, this naive method only provides data at the coordinates of activated temperature sensors. The second approach is the output of Algorithm 1, the estimated belief state of the entire environment at each timestep. The characterization methods are evaluated through performance metrics detailed in Section III-A. The setup of this environment, the creation of the ersatz ground-truth fires, and the arrangement of the temperature and vision sensor sets are given in Section III-B. The performances of the estimators are compared in Section III-C.

A. Large-Scale Performance Metrics

The perimeter estimate g^k assesses the estimated fire shape in regard to its extents compared to some true fire boundary, while the representation error $\varepsilon^{(k)}$ rewards the estimate for assigning higher beliefs at the correct locations (and penalizes for incorrect belief assignments).

Consider a single ignition point at coordinate $(i,j)^*$ and time $k = 0$. Furthermore, for all succeeding times $k > 0$, consider the boundary ∂C representing the outer edge of the actual burned area C. The polar coordinate $r^{(k)}(\varphi)$ gives the radial distance from the ignition point to the point on ∂C at the angle $\varphi \in [0, 2\pi]$ at time k. Thus, given the set of N rays at time k emanating from the ignition point over the set of angles $\Phi = \{\varphi_1, \ldots, \varphi_j, \ldots, \varphi_N\}$, a discretized representation of the wildland fire object is given as the set of radials $R^{(k)} = \{r^{(k)}(\varphi_1), \ldots, r^{(k)}(\varphi_j), \ldots, r^{(k)}(\varphi_N)\}$. A simulated fire

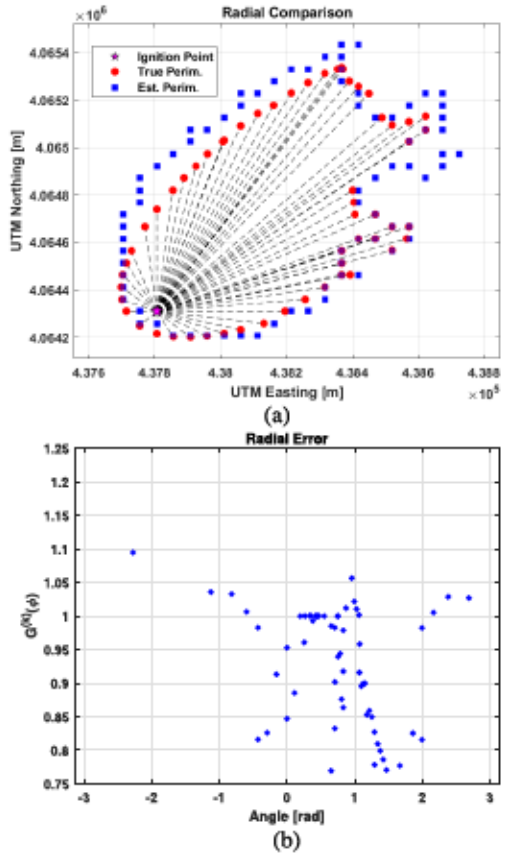

Fig. 9. (a) Example of overlaid radials (the red set treated as the truth) and the resulting radial errors $G^{(k)}(\varphi, \Upsilon = 0)$ at each angle in (b).

from the same ignition point whose burning (or burned) area at time k is given as D with boundary ∂D and represented as a radial set computed over the set of identical angles $\tilde{R}^{(k)} = \{\tilde{r}^{(k)}(\varphi_1), \ldots, \tilde{r}^{(k)}(\varphi_j), \ldots, \tilde{r}^{(k)}(\varphi_N)\}$, where $\tilde{r}^{(k)}(\varphi)$ gives the radial distance from the ignition point to the point on ∂D. Given the radial sets for the actual fire $R^{(k)}$ and the simulated fire $\tilde{R}^{(k)}$ at time k, a method given by Fujioka [57] evaluates the radial performance error at each angle φ

$$G^{(k)}(\varphi) = \frac{r^{(k)}(\varphi_j)}{\tilde{r}^{(k)}(\varphi_j)}, \quad \tilde{r}^{(k)}(\varphi_j) > 0.$$

In this work, we are not concerned with the radial set of a single simulation but rather the range of possible perimeters at each time given the probabilistic belief state. Thus, we modify this radial error metric by introducing a *confidence threshold value* $\Upsilon \in [0, 1)$ such that we can generate an estimated area D as the compact boundary of all burned locations $\sum_{A \in \{F,S,\{F,S\}\}} m(A) > \Upsilon$, which gives a simulated radial set dependent on Υ, $\tilde{R}^{(k)}(\Upsilon) = \{\tilde{r}^{(k)}(\varphi_1, \Upsilon), \ldots, \tilde{r}^{(k)}(\varphi_j, \Upsilon), \ldots, \tilde{r}^{(k)}(\varphi_N, \Upsilon)\}$. This leads to the modified, Υ-dependent, radial error

$$G^{(k)}(\varphi, \Upsilon) = \frac{r^{(k)}(\varphi_j)}{\tilde{r}^{(k)}(\varphi_j, \Upsilon)}, \quad \tilde{r}^{(k)}(\varphi_j, \Upsilon) > 0. \tag{21}$$

Fig. 9(a) shows two example perimeters cast as radial sets with $\Upsilon = 0$. Fig. 9(b) depicts the radial errors $G^{(k)}$ of this estimated area D over a set of angles. A threshold value of $\Upsilon = 0$ will yield all (estimated) feasible locations of the burned area, whereas setting $\Upsilon = 0.9$ will give a tighter (but more confident) perimeter from which to work from. To encapsulate this metric per time instance, we employ (21) and compute the mean radial performance error over the entire angle set Φ

$$g^{(k)}(\Upsilon) = \frac{1}{|\Phi|} \sum_{\varphi_j \in \Phi} G^{(k)}(\varphi, \Upsilon). \tag{22}$$

A mean radial error value of $g^{(k)}(\Upsilon) = 1$ is desired, as it means that the estimate neither "overshoots" nor "undershoots" the entire extent of the fire perimeter. The second metric arises from the need to gauge the precision of the estimated state at every location. We adopt the use of pignistic probabilities from (5) and propose the following *representation* performance metric:

$$\varepsilon^{(k)} = \frac{1}{m \times n} \sum_{i=1}^{m} \sum_{j=1}^{n} \left(1 - P_{\text{Bet}}^{(k)}(\theta)\right), \quad \text{where } \mathbb{S}^{(k)}(i, j) = \theta. \tag{23}$$

The subtraction ensures that a higher belief in an incorrect state will incur a penalty. Furthermore, it does not penalize belief allocated completely to ignore the same as it would to belief allocated completely to the incorrect state. A perfect estimation across every location will yield values of $\varepsilon^{(k)} = 0$ at every timestep, and $\varepsilon^{(k)} = 1$ for a completely incorrect representation.

B. Simulation Setup

The simulation environment was a square 2.5 km × 2.5 km landscape modeled after a Taos County, New Mexico region, where the Rio Grande river is situated between two mountains (Cerro Chiflo to the northwest and the Guadalupes to the southeast). This area was chosen as a testbed due to its changing elevation and variety of combustible fuel types. Vegetation and elevation data from [58] and [59] were collated to provide appropriate fuel and slope inputs, as shown in Fig. 10. Two fuel types were adopted from the models developed by [60]: 1) the very high load, dry climate shrub [denoted SH7, the orange locations in Fig. 10(b)] and 2) the very high load, dry climate timber shrub [denoted TU5, the green locations in Fig. 10(b)]. A "D2L2" moisture content scenario was universally adopted for both fuel models, as described in Table I. The spread rates and flame lengths for both models are shown in Fig. 11.

Two separate wildland fire events were numerically simulated. The first simulation (denoted "Scenario I") was based on average wind records near Taos on April 10, 2019, at 6 A.M. and featured calm (i.e., low wind speed) and no variation in wind direction. Scenario I featured a single ignition point at UTM Easting and Northing [437 806.12 m, 4 064 310.20 m]. The second simulation (denoted "Scenario II") was again based on average wind records near Taos on April 10, 2019, but at 2 P.M. where wind velocities are more volatile in both speed and direction. The differing wind conditions are given in Table II. Similar to Scenario I, a single ignition point was set

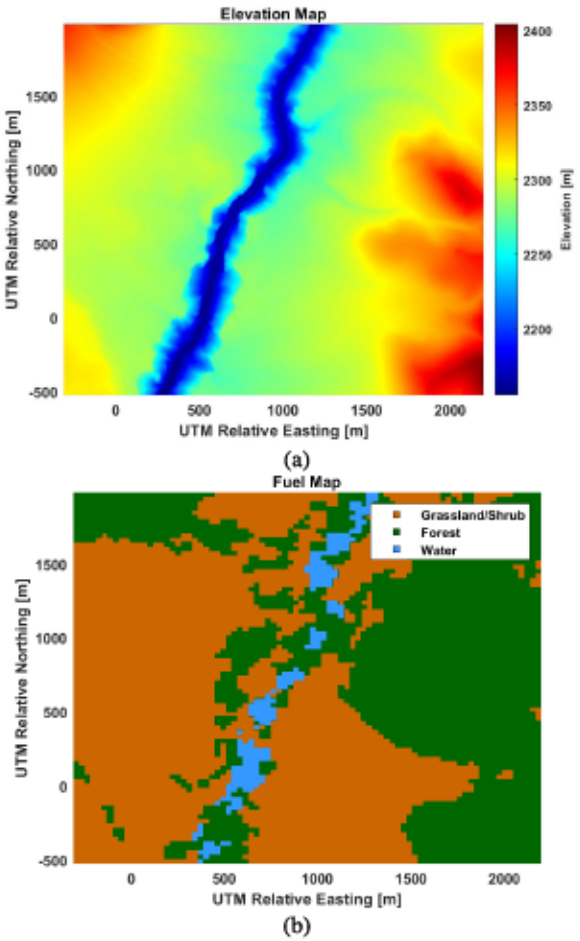

Fig. 10. (a) Slope and (b) fuel information at discretized spatial locations within the simulation testbed.

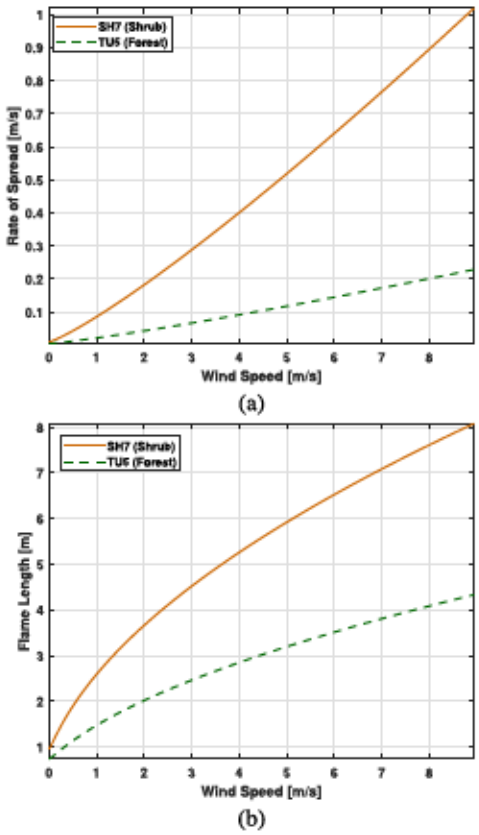

Fig. 11. Effect of midflame wind speed on (a) fire's head rate of spread and (b) flame length.

TABLE I
LIVE AND DEAD FUEL MOISTURE CONTENTS AT AMBIENT TEMPERATURE: 25 °C

Fuel Type	Moisture
Dead 1-hr	6%
Dead 10-hr	7%
Dead 100-hr	8%
Live Herbaceous	60% (2/3 Cured)
Live Woody	90%

TABLE II
MIDFLAME WIND CONDITIONS FOR WILDLAND FIRE SIMULATIONS

Property ↓	Scenario I (Calm)	Scenario II (Erratic)
Direction	SW	{W,SW,S}
Min. Speed [m/s]	1.79	4.47
Max. Speed [m/s]	3.13	8.05

at UTM Easting and Northing [437 806.12 m, 4 064 310.20 m] and supplied to the forecaster, but a second fire (unbeknownst to the forecaster) was ignited 30 min later at UTM Easting and Northing [439 100 m, 4 064 500 m]. Using the given wind, fuel, and slope conditions, a single instance of the MTT algorithm was run for both scenarios over a simulation time of 2 hours. By discretizing a fire perimeter's location and associated flame heights at timesteps of 30 s, we, respectively, characterize the "ground-truth" fires of Scenarios I and II at any time k as $\Delta_{\mathrm{I}}^{(k)}$ and $\Delta_{\mathrm{II}}^{(k)}$. The fire perimeters at increasing times for both scenarios are shown in Fig. 12. The reasoning behind two simulated ground-truth fires (and, therefore, two separate estimation simulations) was to contrast the wildfire characterization performance of both estimations between: 1) correct environmental inputs for Scenario I and 2) incorrect environmental inputs for Scenario II. For Scenario II, these faulty environmental inputs were incorporated by supplying the forecaster with a maximum wind speed that was too low (6.7 m/s instead of 8.05 m/s) and the assumption that the wind direction in each location would not change from a northeast heading. The locations and times of ignition for the fires in both scenarios were not provided to the estimation algorithm.

A simulated wireless network of 200 temperature sensors was randomly distributed across the landscape in a uniform manner, each of which reported ambient temperature readings based on the simulated radiative heating induced by nearby fire front locations at each timestep. Six aerial sensors were deployed from a charging base at UTM Easting and Northing [438 000 m, 4 066 000 m] in cascading release order and surveyed the environment at a constant elevation of 120 m. Each vision agent observed a simulated image $\mathbb{I}^{(k)}(i, j)$ comprised of pixel variables drawn from the true state's corresponding

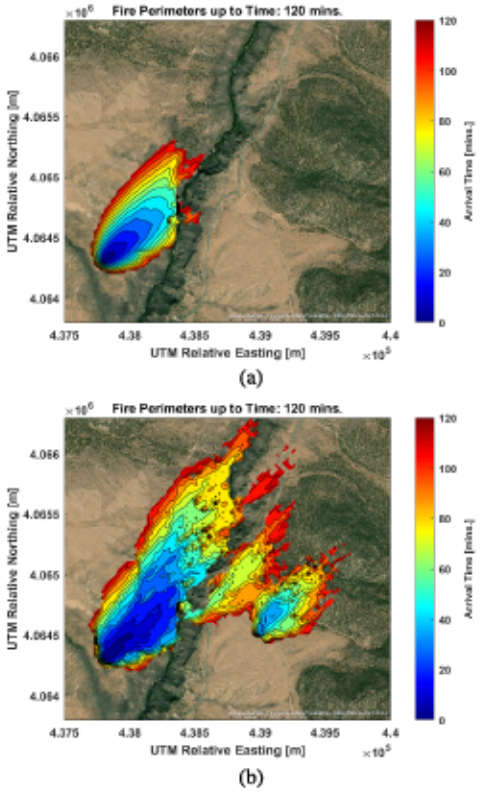

Fig. 12. Simulated ground-truth fires for (a) Scenario I and (b) Scenario II.

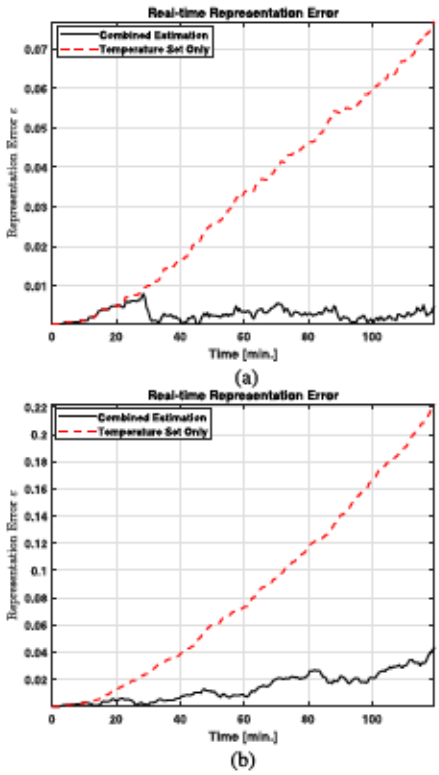

Fig. 13. Representation errors between the belief state estimates of $\Xi^{(k)}$ and $\mathbf{B}_{\mathrm{C}}^{(k)}$ are shown for (a) Scenario I and (b) Scenario II. The black dashed line at every time represents the representation error of the ground-truth $\Delta^{(k)}$.

bivariate distribution $\mathbf{p}^{(k)}(u, v) \sim \mathcal{N}_\theta(\hat{\mathbf{p}}_\theta, \mathbf{C}_\theta)$. Each drone was allowed a maximum time of flight of 30 min before a return command was issued, at which point the agent was required

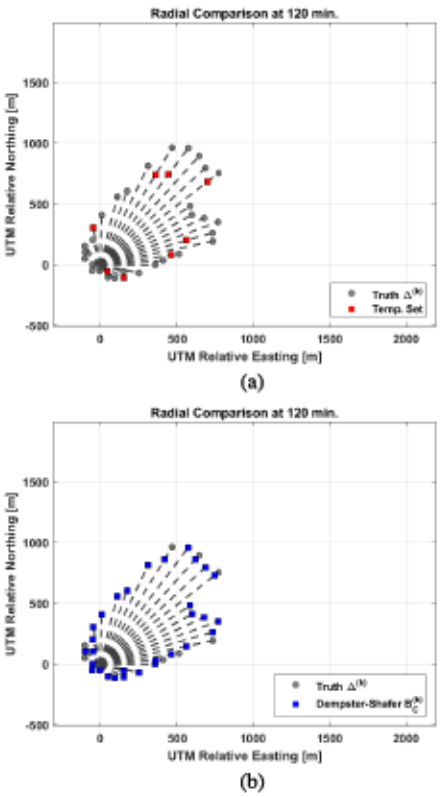

Fig. 14. Convex hull of activated temperature agents (red perimeter) and belief estimate $\sum_{A\in\{F,S,[F,S]\}} m(A) \geq 0.75$ (blue perimeter) in Scenario I. (a) Temperature sensor set. (b) DST estimate.

to autonomously charge before continuing its surveillance tasks. It was assumed that all temperature and vision agents can communicate their information from any position to a central ground station located near the aerial agent's charging base without latency or bandwidth limitations, and the estimation procedure was enacted at each timestep according to Algorithm 1 laid out in Section II-D.

C. Comparative Estimation Performance

The estimation performance metrics derived in Section III-A were computed over all timesteps for the following characterization approaches.

1) *Temperature Agent Set:* The collection of individual beliefs $\mathbf{m}_{\mathrm{T}}^{(k)}$ of all activated temperature sensors within the sensor network $\mathbb{T}^{(k)}$ at timestep k provides a primitive depiction of which locations the fire disturbance has traveled through.
2) *DST Combination:* Given a set of environmental parameters and a network of sensing agents, this estimate is generated through the bidirectional procedure described in Section II-D. The forecasting step is achieved by propagating the fire dynamics over a series of 50 Monte Carlo runs. The belief state estimate at each time is represented as the matrix of combined mass number arrays $\mathbf{B}_{\mathrm{C}}^{(k)}$.

To evaluate the performances of both the temperature set $\mathbb{T}^{(k)}$ and the evidential estimate $\mathbf{B}_{\mathrm{C}}^{(k)}$, the mass number arrays

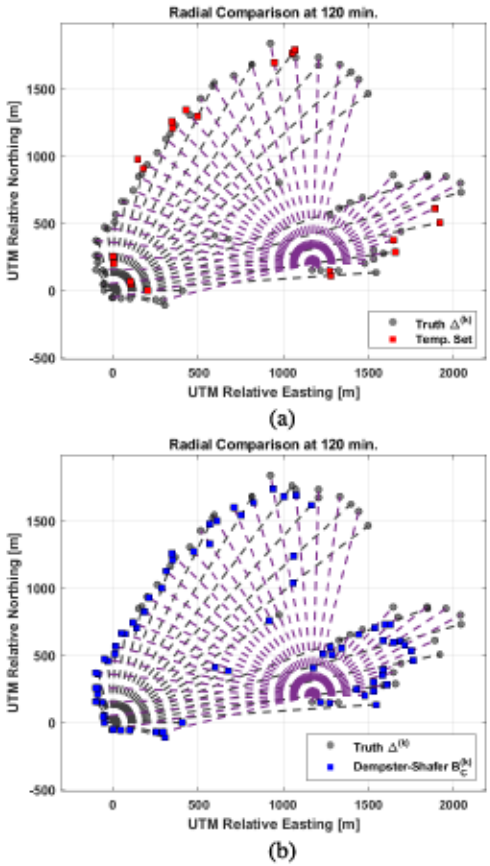

Fig. 15. Convex hull of activated temperature agents (red perimeter) and belief estimate $\sum_{A\in[F,S,[F,S]]} m(A) \geq 0.75$ (blue perimeter) in Scenario II. (a) Temperature sensor set. (b) DST estimate.

used were, respectively, $\mathbf{m}_{\mathrm{T}}^{(k)}$ and $\mathbf{m}_{\mathrm{C}}^{(k)}$ at each applicable location (i, j).

1) Representation Error: The representation error $\varepsilon^{(k)}$ of each belief state estimate of both ground-truth fires $\Delta_{\mathrm{I}}^{(k)}$ and $\Delta_{\mathrm{II}}^{(k)}$ is shown in Fig. 13(a) and (b), respectively. In both scenarios, the performances of the temperature set (red dashed line) and evidential estimates (black line) are largely indistinguishable early in the simulation, as the fire is relatively small when it is first observed. However, as the fire disturbance grows over time, the error of the temperature set increases substantially more than the evidential estimate. This is due to the inherent disparity between the two approaches: while the estimator provides beliefs for all locations, the temperature set must contend with an expanding boundary. This error trend is also observed (albeit much less dramatic) for the evidential estimator in Scenario II. This is likely due to the expanding fire border as above, as well as the choice of cascading release order for the drones.

2) Radial Error: The mean radial errors $g^{(k)}(\Upsilon)$ for both methods were computed at a confidence threshold value of $\Upsilon = 0.75$ and simulation ending time of 120 min. In general, these results support the patterns exhibited by the comparison of representation error $\varepsilon^{(k)}$ above and are tabulated in Table III.

In contrast to the representation error discussed above, a value of $g^{(k)}(\Upsilon) = 1$ is desired. The low mean radial error

TABLE III
MEAN RADIAL ERROR $g^{(k)}(\Upsilon)$

Method ↓	Scenario I (Calm)	Scenario II (Erratic)
Temperature Set	0.326	0.226
Evidential Estimator	0.959	1.26

quantities produced by the temperature set are apparent in Figs. 14 and 15. In situations where no temperature sensor lies along a ray emanating from the ignition point at an angle φ [e.g., the northwest perimeter in Fig. 14(a)], then a value of $G^{(k)}(\varphi, \Upsilon) = 0$ is assigned, which drives down the mean radial error in the aggregate. Both methods displayed increased radial error in Scenario II compared to Scenario I.

IV. CONCLUSION

A review of the results in Section III supports the premise that has been alluded to throughout this work: that belief state estimation via evidential reasoning will yield a superior representation of an evolving wildland fire even when in the presence of deficient prior beliefs, particularly those caused by errant wind behaviors and additional ignitions. There are a number of potential studies that can improve this work as it currently stands. We have identified three major avenues of further research.

1) *Experimental Validation:* There has been substantial work done already to carry out the estimation procedure described in this work during a prescribed burn scenario in order to test its current characterization capabilities. Undoubtedly, new ideas and further improvements to address the needs of first responders and fire suppression personnel will come about from further in-the-field studies.
2) *Vision Agent Improvements:* During a wildfire event, there are numerous hazards that can be encountered by a drone, including thermal radiation, wind gusts, and airborne obstacles, such as embers or other aerial agents. Thus, we require autonomously generated paths for the drones that are robust, time-efficient, and adaptive to incoming information en route to their assigned locations. While visible images were modeled in this work, thermal images (where pixels indicate differences in infrared radiation) may provide better observations by eliminating smoke obscuration and the ambiguous pixels that indicate both fire and vegetation simultaneously.
3) *Fire Forecasting Updates:* In its current form, the forecaster is adaptive in the sense that it allows the propagation of fire from originally unforeseen locations although the range of inputs that drive the dynamics of *how* the fire propagates is invariant throughout the estimation scenario. In other words, the range of wind speeds, wind directions, fuel type, and fuel moisture does not change. In an actual wildfire scenario, however, wind velocities are dynamic across a complex landscape. Thus, it will be beneficial to update the fire dynamic inputs from incoming measurements (e.g., the vision

sensor can provide images from which the predominant smoke (i.e., wind) direction is determined).

REFERENCES

[1] A. L. Westerling, H. G. Hidalgo, D. R. Cayan, and T. W. Swetnam, "Warming and earlier spring increase western U.S. Forest wildfire activity," *Science*, vol. 313, no. 5789, pp. 940–943, Aug. 2006.

[2] J. Douglas *et al.*, *Federal Wildland Fire Management Policy, 1995: Review and Update*. Washington, DC, USA: U.S. Dept. Interior, U.S. Dept. Agricult., 2001.

[3] D. Thomas, D. Butry, S. Gilbert, D. Webb, and J. Fung, "The costs and losses of wildfires," NIST, Gaithersburg, MA, USA, Tech. Rep., SP-1215, 2017.

[4] M. F. Kinnaird and T. G. O'Brien, "Ecological effects of wildfire on lowland rainforest in Sumatra," *Conservation Biol.*, vol. 12, no. 5, pp. 954–956, Oct. 1998.

[5] M. S. Crowther, A. I. Tulloch, M. Letnic, A. C. Greenville, and C. R. Dickman, "Interactions between wildfire and drought drive population responses of mammals in coastal woodlands," *J. Mammal.*, vol. 99, no. 2, pp. 416–427, Apr. 2018.

[6] B. Bass *et al.*, "Lower north fork prescribed fire: Prescribed fire review," State Colorado Dept. Natural Resour., Denver, CO, USA, Tech. Rep., 2012.

[7] M. R. B. November and M. Keelty, *Appreciating the Risk: Report of the Special Inquiry into the November 2011 Margaret River Bushfire*. West Perth. WA, Australia: Government of Western Australia, 2012.

[8] *Wildland Fire Incident Management Field Guide: PMS 210*, National Wildfire Coordinating Group, Washington, DC, USA, 2013.

[9] J. L. Crassidis and J. L. Junkins, *Optimal Estimation of Dynamic Systems*. Boca Raton, FL, USA: CRC Press, 2011.

[10] W. L. Fons, "Analytical considerations of model forest fires," M.S. thesis, Dept. Mech. Eng., Univ. California, Berkeley, CA, USA, 1940.

[11] W. L. Fons, "Analysis of fire spread in light forest fuels," *J. Agricult. Res.*, vol. 72, no. 3, p. 93, 1946.

[12] R. C. Rothermel, *A Mathematical Model for Predicting Fire Spread in Wildland Fuels*. Washington, DC, USA: Intermountain Forest Range Exp. Station, Forest Service, 1972, vol. 115.

[13] F. A. Albini, *Computer-Based Models of Wildland Fire Behavior: A User's Manual*. Washington, DC, USA: Intermountain Forest Range Exp. Station, Forest Service, 1976.

[14] F. A. Albini, *Estimating Wildfire Behavior and Effects*, vol. 30. Washington, DC, USA: Dept. Agricult., Forest Service, Intermountain Forest Range Exp. Station, 1976.

[15] W. Hargrove, R. Gardner, M. Turner, W. Romme, and D. Despain, "Simulating fire patterns in heterogeneous landscapes," *Ecol. Model.*, vol. 135, nos. 2–3, pp. 243–263, Dec. 2000.

[16] E. Catchpole, T. Hatton, and W. Catchpole, "Fire spread through nonhomogeneous fuel modelled as a Markov process," *Ecol. Model.*, vol. 48, nos. 1–2, pp. 101–112, 1989.

[17] D. Boychuk, W. J. Braun, R. J. Kulperger, Z. L. Krougly, and D. A. Stanford, "A stochastic forest fire growth model," *Environ. Ecol. Statist.*, vol. 16, no. 2, pp. 133–151, Jun. 2009.

[18] Z. L. Krougly, I. F. Creed, and D. A. Stanford, "A stochastic model for generating disturbance patterns within landscapes," *Comput. Geosci.*, vol. 35, no. 7, pp. 1451–1459, Jul. 2009.

[19] A. L. Sullivan, "Wildland surface fire spread modelling, 1990–2007. 1: Physical and quasi-physical models," *Int. J. Wildland Fire*, vol. 18, no. 4, pp. 349–368, Jun. 2009.

[20] A. L. Sullivan, "Wildland surface fire spread modelling, 1990–2007. 2: Empirical and quasi-empirical models," *Int. J. Wildland Fire*, vol. 18, no. 4, pp. 369–386, Jun. 2009.

[21] A. L. Sullivan, "Wildland surface fire spread modelling, 1990–2007. 3: Simulation and mathematical analogue models," *Int. J. Wildland Fire*, vol. 18, no. 4, pp. 387–403, Jun. 2009.

[22] M. E. Alexander and M. G. Cruz, "Limitations on the accuracy of model predictions of wildland fire behaviour: A state-of-the-knowledge overview," *Forestry Chronicle*, vol. 89, no. 3, pp. 372–383, Jun. 2013.

[23] T. Srivas, T. Artés, R. A. de Callafon, and I. Altintas, "Wildfire spread prediction and assimilation for FARSITE using ensemble Kalman filtering," *Proc. Comput. Sci.*, vol. 80, pp. 897–908, Jan. 2016.

[24] D. M. Doolin and N. Sitar, "Wireless sensors for wildfire monitoring," *Proc. SPIE*, vol. 5765, pp. 477–484, May 2005.

[25] K. Govil, M. L. Welch, J. T. Ball, and C. R. Pennypacker, "Preliminary results from a wildfire detection system using deep learning on remote camera images," *Remote Sens.*, vol. 12, no. 1, p. 166, Jan. 2020.

[26] H. X. Pham, H. M. La, D. Feil-Seifer, and M. Deans, "A distributed control framework for a team of unmanned aerial vehicles for dynamic wildfire tracking," in *Proc. IEEE/RSJ Int. Conf. Intell. Robots Syst. (IROS)*, Sep. 2017, pp. 6648–6653, doi: 10.1109/IROS.2017.8206579.

[27] E. Zervas, A. Mpimpoudis, C. Anagnostopoulos, O. Sekkas, and S. Hadjiefthymiades, "Multisensor data fusion for fire detection," *Inf. Fusion*, vol. 12, no. 3, pp. 150–159, Jul. 2011.

[28] J. Zhao, Y. Liu, Y. Cheng, Y. Qiang, and X. Zhang, "Multisensor data fusion for wildfire warning," in *Proc. 10th Int. Conf. Mobile Ad-hoc Sensor Netw.*, Dec. 2014, pp. 46–53.

[29] C. González, M. Castillo, P. García-Chevesich, and J. Barrios, "Dempster-Shafer theory of evidence: A new approach to spatially model wildfire risk potential in central Chile," *Sci. Total Environ.*, vols. 613–614, pp. 1024–1030, Feb. 2018.

[30] G. Wang, Y. Zhang, W.-F. Xie, and Y. Qu, "Unsupervised detection for burned area with fuzzy C-means and D-S evidence theory," in *Proc. 2nd Int. Conf. Ind. Artif. Intell. (IAI)*, Oct. 2020, pp. 1–5.

[31] A. A. Soderlund and M. Kumar, "Markovian wildfire modeling via evidential reasoning," in *Proc. IEEE Conf. Decis. Control (CDC)*, Dec. 2018, pp. 5592–5597.

[32] A. A. Soderlund, M. Kumar, and C. Yang, "Autonomous wildfire monitoring using airborne and temperature sensors in an evidential reasoning framework," in *Proc. AIAA Scitech Forum*, Jan. 2019, p. 2263.

[33] A. A. Soderlund, M. Kumar, and R. Aggarwal, "Estimating the real-time spread of wildfires with vision-equipped UAVs and temperature sensors via evidential reasoning," in *Proc. AIAA Scitech Forum*, Jan. 2020, p. 1197.

[34] T. Denoeux, "A neural network classifier based on Dempster-Shafer theory," *IEEE Trans. Syst., Man, Cybern., A, Syst. Humans*, vol. 30, no. 2, pp. 131–150, Mar. 2000.

[35] M. Bauer, "Approximation algorithms and decision making in the Dempster-Shafer theory of evidence—An empirical study," *Int. J. Approx. Reasoning*, vol. 17, nos. 2–3, pp. 217–237, Aug. 1997.

[36] A. D. Jaunzemis, M. J. Holzinger, and M. K. Jah, "Evidence-based sensor tasking for space domain awareness," in *Proc. Adv. Maui Opt. Space Surveill. Technol. Conf.*, Maui Econ. Develop. Board, Maui, HI, USA, 2016, p. 33.

[37] K. Sentz and S. Ferson, "Combination of evidence in Dempster-Shafer theory," Sandia Nat. Laboratories, Albuquerque, NM, USA, Tech. Rep. SAND2002-0835, vol. 4015, 2002.

[38] L. A. Testa, C. D. Pickle, and S. S. Blackman, "A Dempster-Shafer approach to multi-sensor track association," in *Proc. IEEE Aerosp. Conf.*, Mar. 2016, pp. 1–9.

[39] E. Blasch, J. Dezert, and B. Pannetier, "Overview of Dempster-Shafer and belief function tracking methods," *Proc. SPIE*, vol. 8745, May 2013, Art. no. 874506.

[40] L. Liu and R. R. Yager, "Classic works of the Dempster-Shafer theory of belief functions: An introduction," in *Classic Works of the Dempster-Shafer Theory of Belief Functions*. Berlin, Germany: Springer, 2008, pp. 1–34.

[41] G. Shafer, "A mathematical theory of evidence turns 40," *Int. J. Approx. Reasoning*, vol. 79, pp. 7–25, Dec. 2016.

[42] G. Shafer, *A Mathematical Theory of Evidence*, vol. 42. Princeton, NJ, USA: Princeton Univ. Press, 1976.

[43] R. R. Yager, "On the Dempster-Shafer framework and new combination rules," *Inf. Sci.*, vol. 41, no. 2, pp. 93–137, Mar. 1987.

[44] D. Dubois and H. Prade, "Representation and combination of uncertainty with belief functions and possibility measures," *Comput. Intell.*, vol. 4, no. 3, pp. 244–264, Sep. 1988.

[45] L. Zhang, "Representation, independence, and combination of evidence in the Dempster-Shafer theory," in *Advances in the Dempster-Shafer Theory of Evidence*. New York, NY, USA: Assoc. Comput. Machinery, 1994, pp. 51–69.

[46] P. Smets and R. Kennes, "The transferable belief model," *Artif. Intell.*, vol. 66, no. 2, pp. 191–234, Apr. 1994.

[47] P. Smets, "The combination of evidence in the transferable belief model," *IEEE Trans. Pattern Anal. Mach. Intell.*, vol. 12, no. 5, pp. 447–458, May 1990.

[48] P. L. Andrews, "The Rothermel surface fire spread model and associated developments: A comprehensive explanation," U.S. Dept. Agricult., Forest Service, Rocky Mountain Res. Station, Fort Collins, CO, USA, Tech. Rep., RMRS-GTR-371, 2018, p. 371.

[49] M. A. Finney, "Fire growth using minimum travel time methods," *Can. J. Forest Res.*, vol. 32, no. 8, pp. 1420–1424, Aug. 2002.
[50] E. W. Dijkstra, "A note on two problems in connexion with graphs," *Numer. Math.*, vol. 1, no. 1, pp. 269–271, Dec. 1959.
[51] R. C. Rothermel, *How to Predict the Spread and Intensity of Forest and Range Fires*, vol. 143. Washington, DC, USA: U.S. Dept. Agricult., Forest Service, Intermountain Forest Range Exp. Station, 1983.
[52] C. Robert and G. Casella, *Monte Carlo Statistical Methods*. New York, NY, USA: Springer, 2013.
[53] D. Drysdale, *An Introduction to Fire Dynamics*. Hoboken, NJ, USA: Wiley, 2011.
[54] B. W. Butler and J. D. Cohen, "Firefighter safety zones: A theoretical model based on radiative heating," *Int. J. Wildland Fire*, vol. 8, no. 2, pp. 73–77, 1998.
[55] P. V. K. Borges and E. Izquierdo, "A probabilistic approach for vision-based fire detection in videos," *IEEE Trans. Circuits Syst. Video Technol.*, vol. 20, no. 5, pp. 721–731, May 2010.
[56] P. C. Mahalanobis, "On the generalized distance in statistics," *Proc. Nat. Inst. Sci. India*, vol. 2, pp. 49–55, Jan. 1936.
[57] F. M. Fujioka, "A new method for the analysis of fire spread modeling errors," *Int. J. Wildland Fire*, vol. 11, no. 4, pp. 193–203, 2002.
[58] *Land Cover Data Download*, USGS, Reston, VI, USA, 2019.
[59] *The National Map Download*, USGS, Reston, VI, USA, 2019.
[60] J. H. Scott, *Standard Fire Behavior Fuel Models: A Comprehensive Set for Use With Rothermel's Surface Fire Spread Model*. Washington, DC, USA: U.S. Dept. Agricult., Forest Service, Rocky Mountain Res. Station, 2005.

Alexander Soderlund (Member, IEEE) received the B.S. degree in aerospace engineering from The University of Texas at Austin, Austin, TX, USA, in 2014, and the Ph.D. degree in aerospace engineering from The Ohio State University, Columbus, OH, USA, in May 2020 under Dr. Mrinal Kumar. His dissertation focused on evidence-based decision-making and real-time state estimation of random dynamical systems.

He was an AFRL Space Scholar in the summers of 2018–2020 and has recently investigated various methods that solve underactuated autonomous rendezvous scenarios between spacecraft. He is currently a Post-Doctoral Research Associate with the National Academy of Sciences, Kirtland Air Force Base, Albuquerque, NM, USA, under the mentorship of Dr. Sean Phillips at the Space Vehicles Directorate of the Air Force Research Laboratory, Kirtland Air Force Base.

Mrinal Kumar (Member, IEEE) received the bachelor's degree in aerospace engineering from IIT Kanpur, Kanpur, India, in 2004, and the Ph.D. degree in aerospace engineering from Texas A&M University, College Station, TX, USA, in 2009.

From 2010 to 2016, he was an Assistant Professor of mechanical and aerospace engineering with the University of Florida, Gainesville, FL, USA. In 2016, his group moved to The Ohio State University, Columbus, OH, USA, where he founded the Laboratory for Autonomy in Data-Driven and Complex Systems. He is currently an Associate Professor with the Department of Mechanical and Aerospace Engineering, The Ohio State University.